PNAS

Supporting Information for

Hydrodynamic Coupling Melts Acoustically Levitated Crystalline Rafts

Brady Wu, Bryan VanSaders, Melody X. Lim, Heinrich M. Jaeger

Brady Wu.
E-mail: bwu34@uchicago.edu

This PDF file includes:

Other supporting materials for this manuscript include the following:

Movies S1 to S5

Supporting Information Text

1. Acoustic Pressure as Function of Frequency and Voltage

We measure the acoustic pressure inside the resonating cavity using a high precision, laser-based optical microphone (Xarion, Eta100 Ultra). The acoustic pressure as a function of driving frequency and voltage V_{pp} applied to the stack of piezoelectric elements above the horn is shown in Fig. S1.

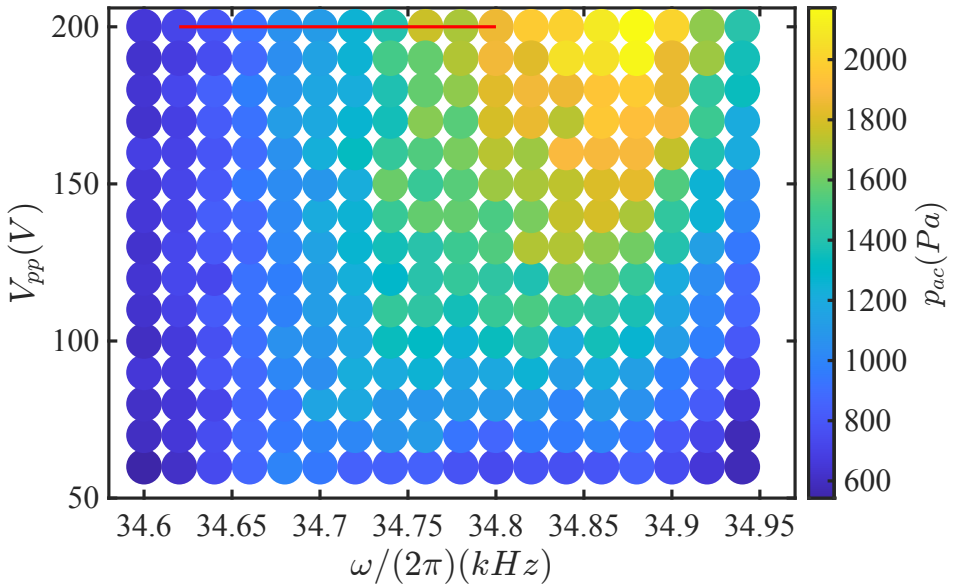

Fig. S1. Cavity acoustic pressure as a function of driving frequency $\omega/(2\pi)$ and voltage V_{pp} applied to the piezo elements. The acoustic pressure is maximized at the resonance frequency ($\omega_0/(2\pi) = 34,870Hz$) and maximum voltage $V_{pp}^{max} = 200$V. The red line corresponds to frequency and voltage parameters used in the experiments reported. The gap size between the transducer and the reflector was kept at $\lambda_0/2$, where $\lambda_0 = 2\pi c/\omega_0 = 9.8mm$.

The distance between the bottom of the acoustic horn and the reflector is fixed at half an acoustic wavelength $\lambda_0/2 = 4.9mm$ (see Fig. 1 in the main text). The resonance frequency of the horn is $\omega_0/(2\pi) = c/\lambda_0 = 34,870Hz$, where c is the speed of sound in air. The acoustic pressure is maximized at the resonance frequency and decreases as the driving frequency is increased or decreased, and it increases monotonically with increasing V_{pp}. The acoustic pressure reported here is an average over 5 repeated measurements. For all experiments discussed in the main text, we adjust the acoustic pressure by fixing V_{pp} at 200V and tuning frequency from 34,620Hz to 34,800Hz (red line in Fig S1). Fixing frequency but changing voltage gives the same experimental behavior, as acoustic pressure is the key parameter for controlling the behavior of experiments reported here.

For the particle size range studied here ($\approx 45\mu m$), large vertical oscillations of the raft center of mass are not observed, unlike the case for $D \approx 200\mu m$ in Ref. (1). Such vertical oscillation instabilities are known to scale with the volume fraction of the resonating cavity occupied by the levitated object (2, 3), and in this study particles are small enough to render the effect negligible. Therefore, the out-of-plane particle fluctuations arising from small ($\Delta\omega/(2\pi) \approx 10Hz$) detuning away from resonance, observed in Ref. (1), are absent here. As a result, even for the comparatively large amounts of detuning across the region shown in Fig. S1 the motions of the small particles stay within the plane of the raft, and the raft as a whole undergoes only small, bounded vertical movements, if it moves at all (as shown in supplementary movie 3).

2. Particle Size Measurement Protocol

Accurately measuring particle diameters is crucial to verifying the predictions by Fabre et al. (4) as well as our LBM simulations of the dependence of the steady-state separation between a pair of particles as a function of Stokes number Ω (Fig. 2E in the main text). This is because Ω depends sensitively on the particle diameter ($\Omega \propto D^2$). Unlike the center-to-center distance, which can be determined accurately for a range of lighting and imaging conditions, the apparent particle diameter in an experimental image will be affected much more by lighting levels and processing protocols. Below, we outline our particle size measurement procedure.

Fig. S2A presents a raw image of a raft as obtained from the high-speed camera. We first perform particle tracking and then zoom in to a region around a selected particle (inset). The radial distance from the center of the particle is defined as r. We then calculate the azimuthally averaged brightness value as a function of r, as shown in Fig. S2B. The brightness decays as we move away from the center of the particle. For $r > 40\mu m$, the brightness increases again due to the presence of neighboring particles (in a manner similar to the radial distribution function, g_r). The black background level in this image has an average brightness value of 10. We take twice the background level as the threshold to determine the particle diameter (orange dashed line in B). According to this protocol, the diameter of the particular particle shown is $60\mu m$. The choice of threshold can

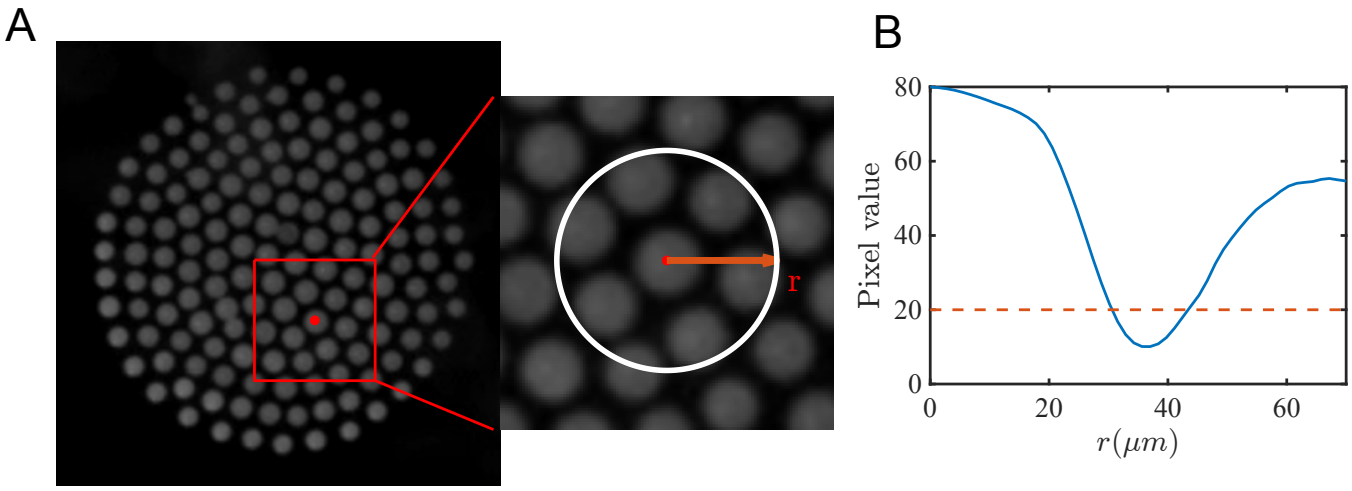

Fig. S2. Protocol for particle size measurement. (*A*) Raw image of a raft and zoomed-in detail showing one particle surrounded by 6 neighbors (inset). r is defined as the radial distance from the center of the particle, as indicated by the white circle. (*B*) Azimuthally averaged pixel brightness value as a function of r for the selected particle in*A*. The orange dashed line represents the cutoff threshold, which we set at twice the brightness value of the (black) background level (brightness value 10 in this image). Pixels within the radius where the azimuthally averaged brightness first crosses the threshold are regarded as part of the particle.

systematically impact the diameter measurement outcome. The diameter measurement therefore has an uncertainty of $5\mu m$ (2 pixels). The error bars corresponding to this uncertainty are plotted for selected data points in Fig. $2E$ of the main text.

3. Particle Size Distribution

We compare the size measurement protocol applied to levitated particles, as described above, to measurements taken with a microscope (OLYMPUS DSX1000) for a representative set of particles on a glass slide. Raw and zoomed-in microscope images for some of these particles are presented in Fig. S3*A*. The microscope imaging system is back-lit and at a higher magnification than the high-speed camera, giving a clear boundary between the particle and the background. The diameter distributions for particles imaged with the high-speed camera and microscope are compared in Fig. S3*B*.

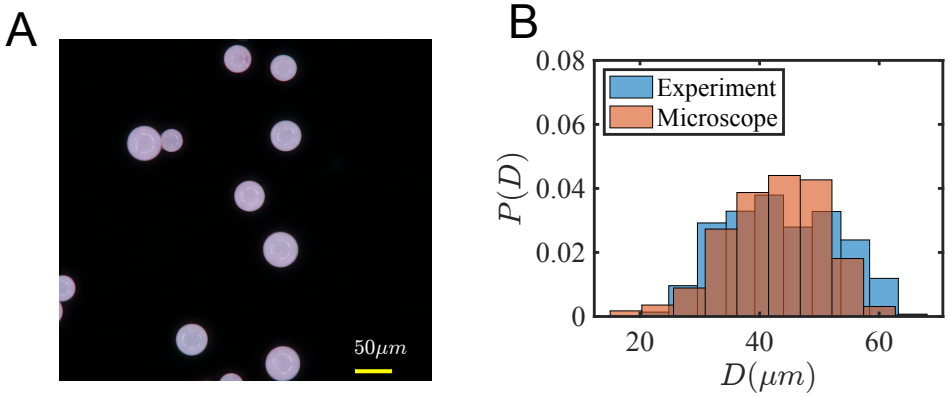

Fig. S3. Particle size distribution. (*A*) Microscope image of a set of particles. (*B*) Diameter distribution of particles extracted from videos of levitation experiments (blue) and from microscope images (orange) in *A*.

The particle size distributions obtained by the two imaging methods agree well. Over 90% of the particles are in the range between $30\mu m$ and $60\mu m$. This distribution is slightly broader than the range $27-45\mu m$ claimed by the manufacturer (Cospheric).

4. Particle Steady-state Separations

The steady-state distances between pairs of particles are presented in Fig. $2E$ of the main text. We point out in the main text that these data contain measurements both on isolated dimers as well as neighboring particles in rafts levitated, and that no significant difference was found between them. To show this directly, Fig. S4 is the same plot of $\langle r \rangle / D$ as a function of Ω, but with data for particles in the raft and isolated dimers plotted in filled and open circles. Different colors stand for the acoustic pressure p_{ac}.

Also shown (dashed line) is the numerical result obtained by Fabre et al. for the steady-state distance of an isolated pair of particles in oscillating flow field. The finding that all data sets overlap implies that, within our experimental accuracy,

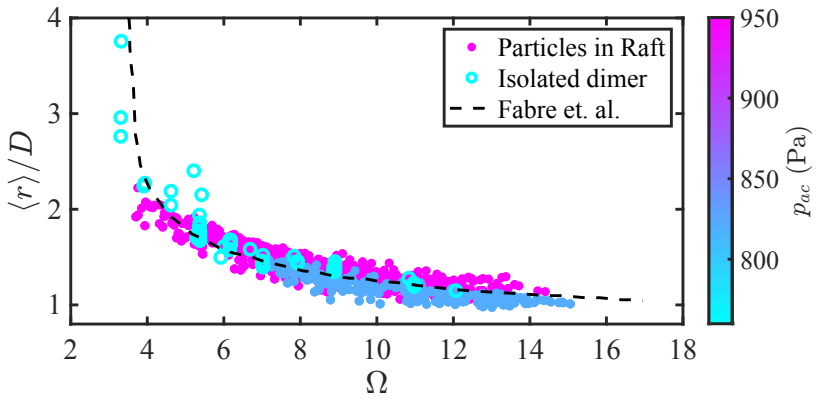

Fig. S4. Comparison of $\langle r \rangle / D$ for pairs of isolated dimers and particles in raft. Steady-state distance normalized by particle diameter, $\langle r \rangle / D$, as a function of the Stokes number, Ω, under different acoustic pressure p_{ac}. Open circles represent isolated dimers, and filled circles are from neighboring particles in rafts. Color denotes different acoustic pressure.

multibody effects can be neglected as far as the steady-state distances between particles are concerned. In addition, the steady-state distance does not change with acoustic pressure, in agreement with our LBM simulation results in Fig. 2*C* and *D* of the main text, where we show that both scattering attraction and streaming repulsion scales with energy density E_0, and thus the steady-state distance is independent of E_0.

5. Structural Properties of the Raft

Figures 1*D* and *F* in the main text show that small particles gather near the edge of the raft and the separation between them seems larger. To quantify this, we first calculate the pair correlation function $g(r)$ for particles at different relative radial position r/R, shown in Fig. S5*A*. We take as the average steady-state separation between particle pair $\langle r \rangle$ as the position of the first peak in $g(r)$. The average steady-state separation $\langle r \rangle$ and the average diameter D of the particles in the raft as a function of relative radial position are shown in Fig. S5*B*. As expected, small particles are sorted and pushed to the raft edge while the steady-state separation between particle pair increases near the raft edge. The increase in $\langle r \rangle$ near the raft edge is due to the decreasing particle size, following the trend in Fig. 2*E* of the main text and in Fig. S4, above. The reason that smaller particles prefer to stay at the raft edge is because this minimizes the area of the raft, which is confined by an effective surface (or line) tension.

To check how the average areal density of particles in the raft depends on energy density, we calculate $N_{raft}/(\pi R^2)$. Here N_{raft} is the total particle number in the raft, and for the time-averaged raft radius R we take the 95th percentile in the radial probability distribution $P(r)$ in Fig. S5*C*. Fig. S5*D* shows that, within measurement accuracy, the areal particle density increases very little with acoustic pressure, if at all.

6. Multi-body Fluid Interactions

In Fig. 3 of the main text, we show that the acoustic interaction forces between a minimal cluster of seven particles are non-reciprocal. The non-reciprocity fundamentally arises because particles interact by exchanging momentum with a surrounding fluid (i.e. hydrodynamics interactions). To illustrate this, we presented a streaming plot in the x-y direction in Fig. 3*C* of the main text. Here, we present a more comprehensive comparison between the fluid flow around a force balanced cluster and the one where the central particle is displaced to the right by $0.3D$.

When the central particle has zero displacement, the streaming flow field around the cluster has six-fold symmetry (Fig. S6*A*-*B*), as expected. Thus, there is no net force on the cluster. Comparing the streaming flow around the cluster at x-y and x-z plane, we note that the stronger streaming flow is above and below the levitation plane. The presence of the cluster also modifies the fluid flow, increasing the local energy density (Fig. S6*C*-*D*).

Displacing the central particle to the right by $0.3D$ breaks the symmetry in x direction and non-trivially changes the flow field within the cluster. As Fig. S6*E* and *F* show, due to the displacement of the central particle, high intensity region around the particle becomes connected and forms bridges. In addition, the displacement of the central particle concentrates the energy density on its right and lowers *E* on its left (Fig. S6*G* and *H*).

7. Velocity Distributions

The velocity distribution of particles within the plane of a levitated cluster depends sensitively on the acoustic pressure, p_{ac}. However, we find that the *form* of the velocity distribution is the same across the full range of acoustic pressure used in the experiments reported here (see red line in Fig. S1).

Figures S7*A* and *B* show the velocity distributions in the levitation plane for the x and y directions at two representative pressures, p_{ac}=848 Pa and 984 Pa. Here the former corresponds to the crystalline state and the latter to the liquid-like phase. The liquid-like distribution conforms closely to the functional form of a granular gas, $P(v) \propto exp(-0.8 * (v/\sqrt{\langle v^2 \rangle})^{3/2})$ (5),

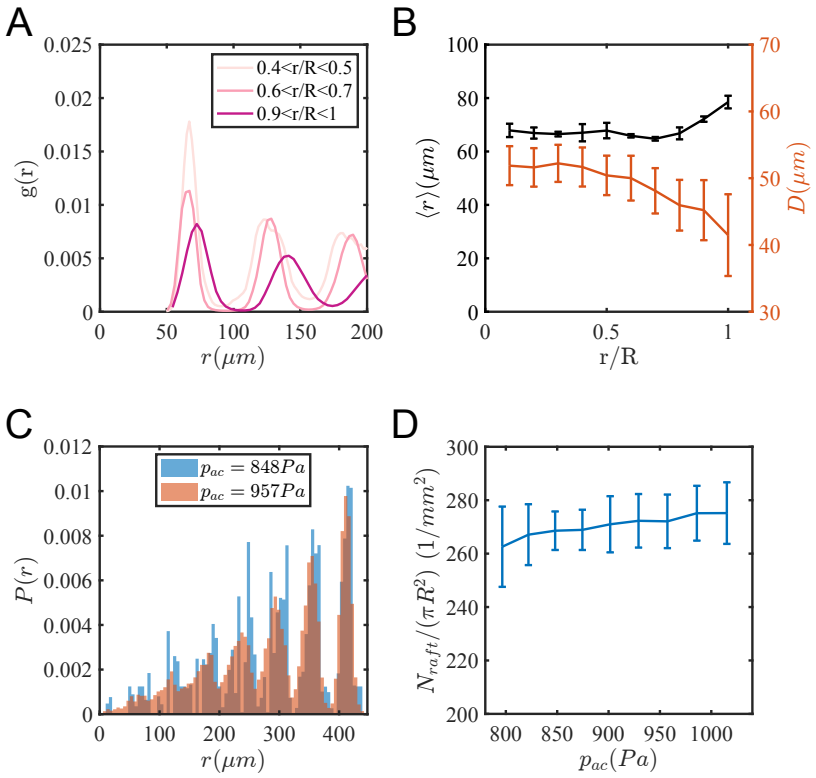

Fig. S5. Structural properties of the raft. (*A*) $g(r)$ for three representative radial position in the raft at $p_{ac} = 848Pa$. The average steady-state distances $\langle r \rangle$ between particles are defined as the position of the first peak in $g(r)$. (*B*) Average steady-state distance between particles $\langle r \rangle$ and the diameters of the particles D as a function of the relative radial position r/R. (*C*) Probability distribution of finding the particles at a given radial distance away from the geometric center of the raft for two representative acoustic pressure p_{ac}. We take for raft radius R the 95 percentile in $P(r)$ from the raft center. (*D*) Number density of the raft as a function of the acoustic pressure p_{ac}. The number density is calculated as $N_{raft}/(\pi R^2)$, where N_{raft} is the total particle number in the raft, and R is the raft radius (see text).

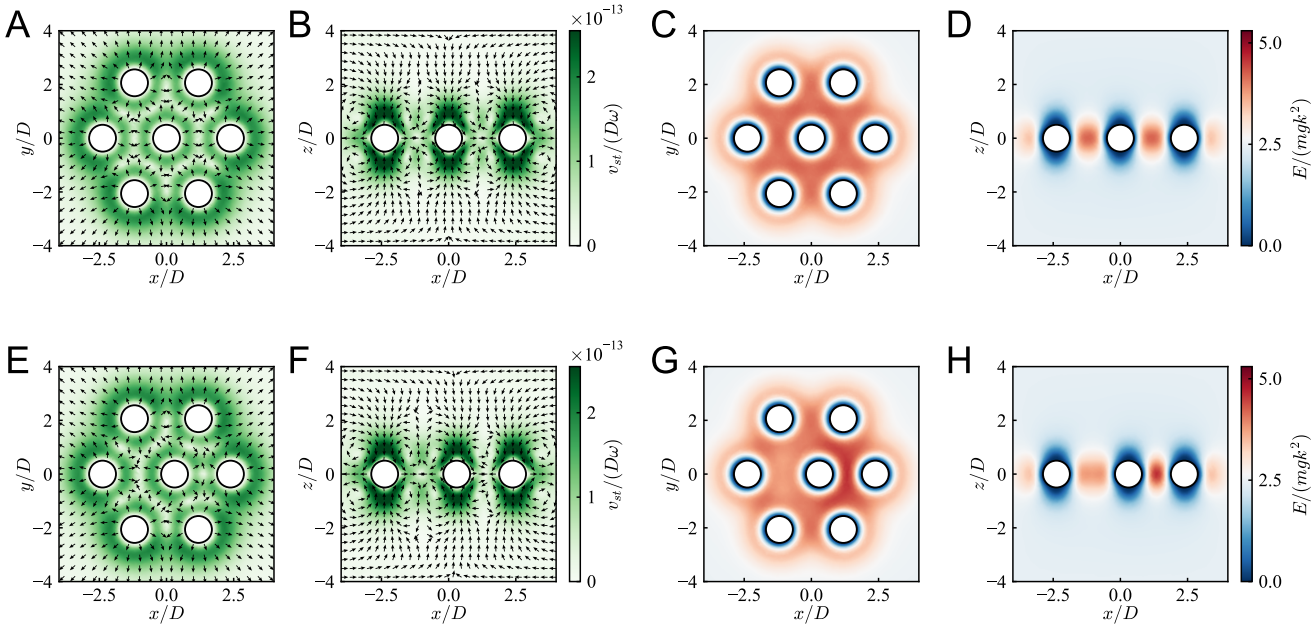

Fig. S6. Multi-body fluid interactions. (*A-D*) Second-order streaming flow and energy density E around a force balanced cluster ($\Delta x/D = 0$) in the x-y plane and x-z plane. The energy density E is normalized by gravitational energy mgk^2, similar to Fig. 3*D* of the main text. (*E-H*) Second-order streaming flow and energy density E around a cluster where the central particle is displaced ($\Delta x/D = 0.3$) in the x-y plane and x-z plane.

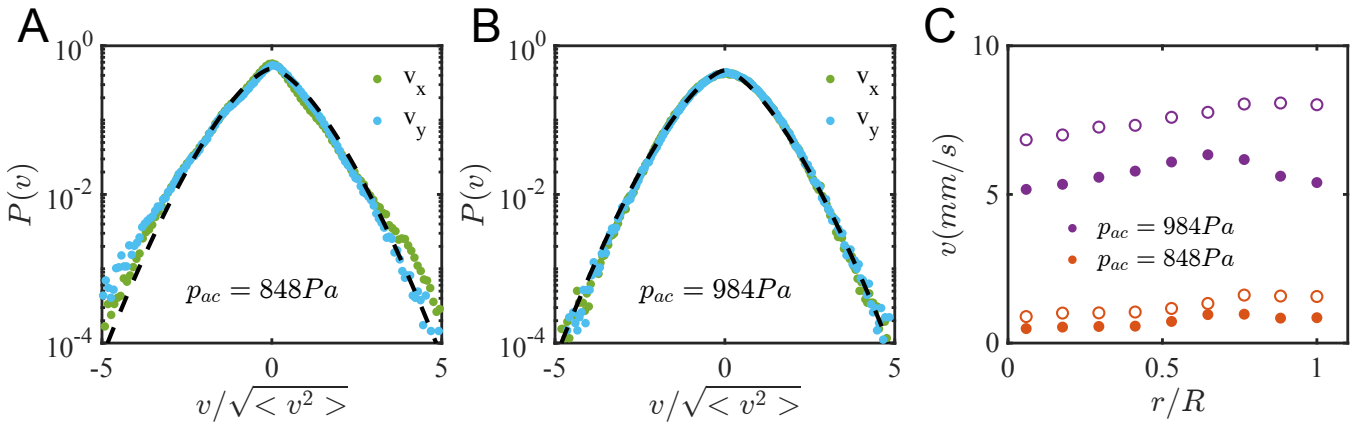

Fig. S7. Velocity distribution of levitated particles. The distribution of x and y components of the particle velocities at sound pressures p_{ac}=848Pa (*A*) and 984 Pa (*B*). The black dashed line corresponds to the typical velocity distribution for a granular gas, $P(v) \propto exp(-0.8 * (v/\sqrt{\langle v^2 \rangle})^{3/2})$ (5). (*C*) Open circles show the average velocity $\langle v \rangle$ of particles in different radial positions, r/R, at p_{ac}=848Pa and 984 Pa; here, $R = D/2$ is the radius of the raft. Filled circles give the average of the difference between individual particle velocity and the average flow in the surrounding background, $\langle v - \langle v_{nn} \rangle \rangle$, where v_{nn} denotes the velocity of nearest neighbor particles.

with equal x and y velocity components indicating isotropy. The raft at $p_{ac} = 848Pa$, which exhibits intermittent dynamics, departs from the granular gas velocity distribution function, particularly in the high-velocity tails.

The average velocity of a particle in the laboratory frame is shown as a function of the radial position, r/R, in Fig. S7*C* (open circles). In the same panel we compare this to the relative velocity of a particle in the moving frame of its nearest neighbor particles, defined as $v - \langle v_{nn} \rangle$, where v_{nn} denotes the velocity of nearest neighbor particles (closed circles). Whereas the average velocity in the laboratory frame increases with r/R linearly, the velocity in the moving frame of neighboring particles is non-monotonic; $\langle v - \langle v_{nn} \rangle \rangle$ peaks around $0.65R$. As will be discussed in section 6, the peak is due to the proliferation of defects around this radial region. The defects mediate between the crystalline triangular lattice in the center and the circular boundary at the edge, lubricating the motion in the azimuthal direction for outer edge particles, as can be observed in the ring-like structure near the raft edge in Fig. 4*A* **ii** of the main text. The collective motion of edge particles in the azimuthal direction then leads to a slightly higher average velocity in the laboratory frame. However, by subtracting the velocity of nearest neighbor particles, we note that the average velocity of the edge particles in the frame of co-moving particles (filled circles) is roughly the same as for the center particles. Thus, while the edge particles exhibit an enhanced average velocity, the collective nature of their motion preserves structural order, as shown in Fig. S8*B*.

8. Radial Dependence of Local Structural Decay Rates

As p_{ac} increases beyond $\approx$ 850 Pa, intermittent excitations melt the crystal-like state into a temporally homogeneous liquid-like state. This liquid-like state displays distinct radial structure in particle displacements, shown in Fig. 4*A* **ii** of the main text, most apparently between the bulk and the edge. To quantify this we calculate the time-averaged order correlation function, $g_6(\Delta t, r) = \langle h_6(t, \Delta t) \rangle_{N_r,t}$ (6), which we average over particles belonging to radial bins (N_r) counted from the raft's center and expressed as a fraction of raft radius, R. For particles near the center of rafts, $r/R < 0.8$, local order decorrelates exponentially in time, in agreement with a classical 2D liquid (6–8), and the characteristic time τ for g_6 to reduce ten-fold is nearly constant: $\tau \approx 10\,ms$ (Fig. S8*A*). However, the outer two layers of the raft are distinctly different, with exponential local order decay at short times, but slow decorrelation at long-times. τ is an order of magnitude larger for the edge particles compared to those at the center of the raft (Fig. S8*B*).

This radial distribution of τ is not present in a thermally fluctuating finite-size particle cluster. To show this we compare our experimental observations to a simulated cluster in a thermal bath using molecular dynamics (9) (green data set in Fig. S8*B*; see section 10 for numerical method details). For comparison between simulated and experimental rafts, the timescale for a particle to cross one lattice spacing in the absence of obstacles (t^*) is used as a normalization. The simulated τ/t^* for a thermally-agitated system *decreases* gently as $r \to R$, opposite the behavior of the experimental levitated raft. This difference is seen qualitatively in the time-averaged images of experimental (Fig. S8*B i*) and simulated rafts (Fig. S8*B* **ii**): the behavior of the edge particles in simulation is qualitatively similar to those in the core, whereas the edge particles in the experiment rarely participate in radial rearrangements and form distinct, ring-like structures.

Fundamentally, this radial dependence is a result of interactions between the moving fluid and the extended body of the raft, coupled with the dependence of HI-driven perturbations on acoustic energy density. To show this we perform a Lattice-Boltzmann simulation of a perfectly crystalline finite-sized raft, with the same spacing as in Fig. 2*E* in the main text. For an arbitrary line of particles in the raft, we can see in Fig. S8*C* that the gaps between particles in the middle of the raft exhibit significantly higher acoustic energy density than those near the edge of the raft. This is because the raft forms an extended barrier to air flow, and this disturbance is least evident at the raft edge, where the air can flow around the raft. From Fig. 4*B* of the main text, p_{ac} directly controls the magnitude of fluctuations. The radial dependence of structural decorrelation in the liquid-like state is partially due to the spatial distribution of the acoustic energy density (and hence

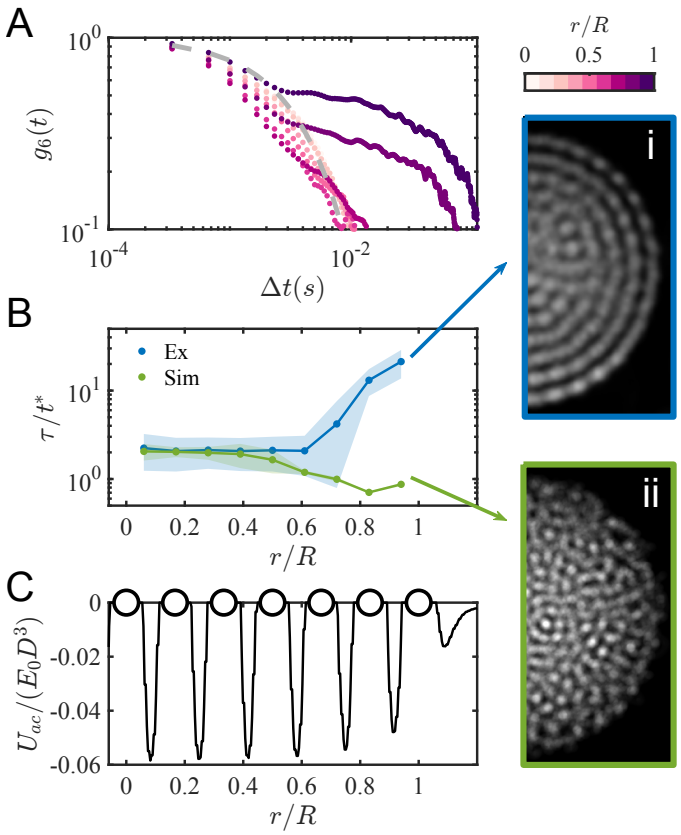

Fig. S8. Radial dependence of local structural decay arising from long range fluid-body interactions. (*A*) $g_6(t)$ for particles at different radial locations r/R within a cluster for $p_{ac} = 957\ Pa$. (*B*) Normalized decorrelation time τ/t^* as a function of r/R, for both the experiment and MD simulation. τ is defined as the time over which g_6 decays to 0.1, and $t^* = L/\langle v \rangle$, where $L = \langle r \rangle$ is the lattice spacing and $\langle v \rangle$ the average velocity. The insets, **i-ii**, show time-averaged images of a raft in the experiment (blue) and in the simulation (green) for $20t^*$. In the experiments, the edge particles rarely rearrange radially and form two distinct rings; the radial structure in simulation is more homogeneous. (*C*) Non-dimensional acoustic energy density as a function of r/R, obtained from a lattice fluid simulation. Here $U_{ac} = \rho v^2/2$, where ρ and v is the density and velocity of the fluid element. White circles represent the positions of particles. The energy density decreases near the cluster edge, due to the interaction of the moving fluid with the extended body of the raft. These effects span the raft, and so are significantly longer-ranged than particle-particle acoustic interactions

HI-driven perturbations), which stems from the fluid-raft interaction that cannot be represented as a sum of independent point scatterers. As this effect depends upon the dimensions of the raft, this fluid-body interaction occurs at length scales considerably longer than the relevant interparticle acoustic interaction. Despite this finite-size effect, we note that the statistics of the intermittent dynamics is the same when only the particles in the raft core are considered (see Fig.S11, below).

9. Particle Motion at Raft Edge

As shown in Fig. 4*A* **ii** and Fig. 5*B* of the main text, particles at the raft edge prefer to move in the azimuthal (ϕ) direction, forming two distinct rings around the edge. To quantify this observation, we calculate the normalized mean squared displacement $\langle(\Delta r/L)^2\rangle$ in radial (r) and azimuthal (ϕ) direction for all particles in the raft (Fig. S9*A*), the bulk ($r < 0.8R$) of the raft (Fig. S9*B*), and the edge ($r > 0.8R$) of the raft (Fig. S9*C*). On average, particles in the raft seem to prefer to move in the ϕ direction. However, a closer look reveals that only the edge particles ($r > 0.8R$) have the tendency to move in the ϕ direction, and the motions of the particles in the bulk ($r < 0.8R$) are isotropic. The tendency for the edge particles to move more freely along the ϕ direction is a consequence of the raft edge acting like a confining wall, which constrains their motion along the radial direction.

The above behavior can be encapsulated in the calculation of $\langle E_{kin} \rangle$ in r and ϕ direction, shown in Fig. S9*D*. The kinetic energy in r and ϕ directions is indistinguishable in the raft bulk but $\langle E_{kin} \rangle$ in ϕ direction is significantly higher at the raft edge, in agreement with the previous results. In addition, the total kinetic energy decreases towards the raft edge, due to the decreasing mass of the smaller particles, but also due to the decreasing energy density around the raft edge, shown in Fig. S8*C*.

10. Defects and Particle Mobility

To understand how the presence of defects impacts the melting of the rafts, we study the decorrelation behavior of g_6, defined as $g_6(\Delta t, r) = \langle h_6(t, \Delta t) \rangle_{N_r,t}$ (6), which we average over particles belonging to radial bins (N_r) calculated from the raft's center and expressed as a fraction of raft radius, R. For all radial positions, g_6 exhibits behavior compatible with algebraic decay for short times ($t < 10^{-2}s$), expressed as a power law of the form $(t/t_c)^{-\alpha}$. This behavior is characteristic of the hexatic

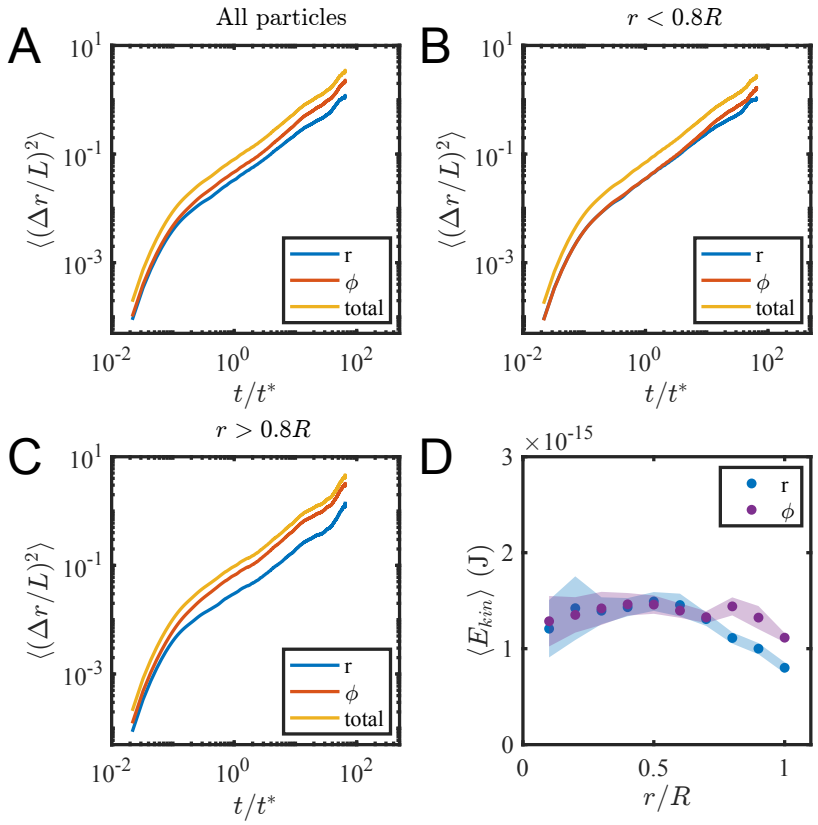

Fig. S9. Particle motion at the raft edge. (*A-C*) Normalized mean squared displacement $\langle(\Delta r/L)^2\rangle$ in r and ϕ direction for all particles in the raft (*A*), the bulk ($r < 0.8R$) of the raft (*B*), and the edge ($r > 0.8R$) of the raft (*C*) at $p_{ac} = 848Pa$. (*D*) Kinetic energy $\langle E_{kin}\rangle = \langle m_i v_i^2/2\rangle_i$ in the ϕ and r direction as a function of the relative radial distance r/R; here m_i and v_i are the mass and velocity of particle i.

phase in classic 2D melting theory (6). Here, t_c is a fitted normalization time scale, and the exponent α reflects the rate of the structural decay.

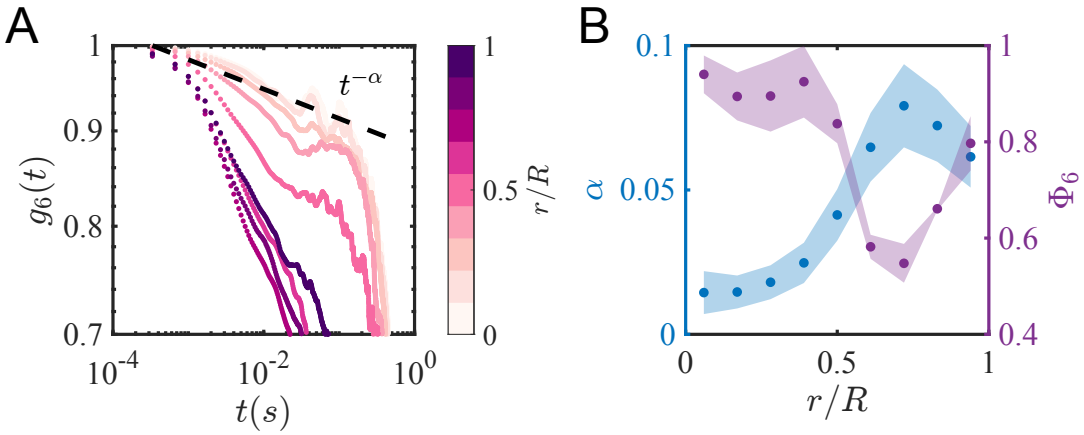

Fig. S10. Defects mediate particle mobility. (*A*) Bond order correlation function $g_6(t)$ as a function of time for particles at different radial position within the cluster, r/R, at $p_{ac} = 848Pa$. The data before $20ms$ can be fit with an algebraic decay, $(t/t_c)^{-\alpha}$. (*B*) Power law exponent α (blue data) and local bond order parameter Φ_6 (purple data) as a function of the relative radial position, r/R.

Figure S10 exemplifies the effect of defects for a raft displaying intermittent dynamics at $p_{ac} = 848Pa$. The data before $20ms$ do not oscillate and can be fit to an algebraic decay, and all traces plummet at $\approx 0.5s$, which is the typical life time of the crystal state before an avalanche takes place. Edge particles have significantly faster decay, but in a non-monotonic way with radial position r/R. The inner core tends to decay slowest, and the decay rate increases with r/R for $r/R < 0.7$. Beyond this, decay rates decrease with r/R.

This non-monotonic trend is quantified by the behavior of the fitted exponent α as a function of r/R (Fig. S10*B*). The non-monotonicity mirrors that of the local order parameter Φ_6, indicating that re-arrangements occur at the greatest rate where

crystalline defects (low Φ_6 values) are present. We conclude that the presence of defects tends to promote particle mobility and rearrangement. This explains the observation that avalanche events typically start with displacements near $r/R \approx 0.7$. Nevertheless, the uncaging behavior and correlated motion involves the entire raft, as shown in section 8.

11. Intermittent Dynamics Considering Only Particles in the Raft Core

The analysis in the prior sections showed that the raft edge does not behave the same as the core, especially in the liquid-like state. To ascertain if intermittent events are also radially inhomogeneous, we calculate the mean-square displacement (MSD), γ, and N_u/N_t for only the particles in the central raft core ($r/R < 0.5$) as a function of time, as shown in Fig. S11. Within experimental uncertainty, we find that results extracted for just the core particles does not differ from the results when we average over all particles in raft, as done for the plots in the main text.

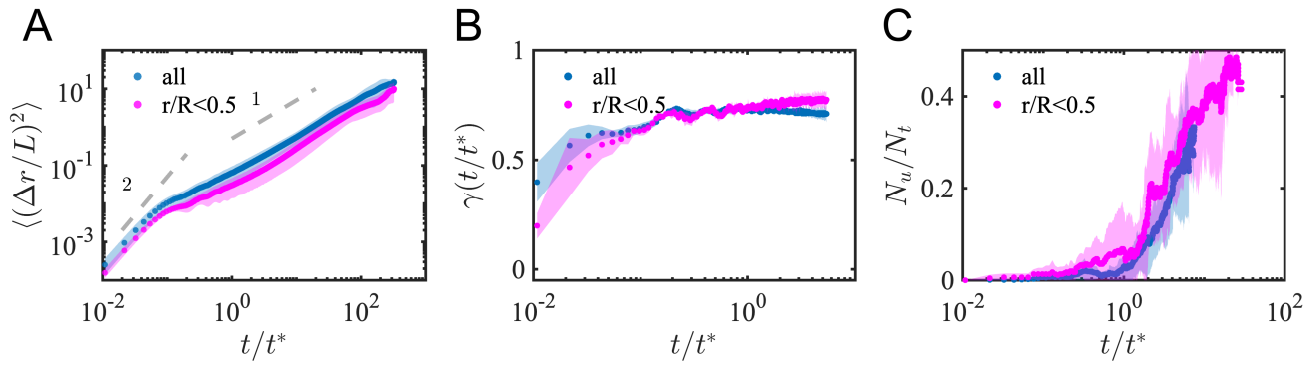

Fig. S11. Bulk and edge particles exhibit the same behavior. (*A*) Normalized mean square displacement $\langle(\Delta r/L)^2\rangle$ as a function of t/t^* for both the bulk particles ($r/R < 0.5$) and all particles. $L = \langle r\rangle$ denotes the lattice spacing, and $t^* = L/\langle v\rangle$. (*B*) γ as a function of normalized time. (*C*) Fraction of uncaged particle in a raft N_u/N_t as a function of normalized time.

12. Long Time Structural Evolution of Intermittent Dynamics

While supercooled liquids and other glassy systems also exhibit intermittent avalanche behavior, we note in the main text that our levitated system does not do so by descending down a rugged configuration landscape and can continue indefinitely. To elaborate on this point, we here present additional structural information for a raft while it undergoes many avalanche events within a time span of 2 seconds.

Figures S12*A* and *B* are the same data as in Fig. 5*A* and Fig. 4*D* of the main text, but plotted out to longer times. We note that there is a clear correspondence between kinetic energy and h_6; when the raft exhibits the intermittent excitation, the local structure also decays, as expected. On the other hand, the local order parameter, Φ_6, does not exhibit a similarly clear correspondence with the data in panels *A* and *B* during avalanches. In general,however, Φ_6 tends to decrease at the beginning of an avalanche and increase at its end. When the raft is in the quiescent state, Φ_6 typically varies little. Importantly, even after many avalanche-type excitations, Φ_6 remains at a similar level, making it clear that the raft is not undergoing a process of avalanche-assisted defect annealing. In particular, the total number of 5,7 defects does not seem to decrease after multiple avalanches, as shown in Fig. S12*D*.

13. MD Simulations

To ascertain the extent to which the properties observed for the rafts in the experiments differ from those expected for a thermal system, we construct a Wigner crystal with repulsive Coulomb interactions. The simulation domain is a 2D rectangle of length $L_{Box} = 300D$, where $D = 2^{1/6}$ is the diameter of a particle. This domain has periodic boundary conditions. The particles interact via a Yukawa potential defined as

$$V_{yukawa}(r) = \epsilon\frac{e^{-\kappa r}}{r}, \qquad [1]$$

where ϵ is a characteristic energy scale and κ^{-1} a characteristic decay length. For all simulation results presented, $\epsilon = 0.5$ and $\kappa = 1$. The Yukawa potential mimics the role of the short-range streaming repulsion in the experiments and keeps the particles away from contact. We place 200 particles in the simulation domain and impose a periodic potential with the form $V(r) = A \times tanh[\frac{1}{2\pi pw}cos(p\vec{b_i}\cdot\vec{r})]$ to confine the particles at the center of the box; here, $p = w = 1$; $b_i = 1/L_{Box}$ is the reciprocal lattice vector; $A = -10/tanh(1/(2\pi pw)) = -63.4$. The size of the simulation box is 5 times the xy dimension of the raft. For regions around the center of the simulation box (and the raft), the confining potential can be approximated by an isotropic harmonic potential with a spring constant $k = 0.0013$. Before each simulation, we thermalize the system with

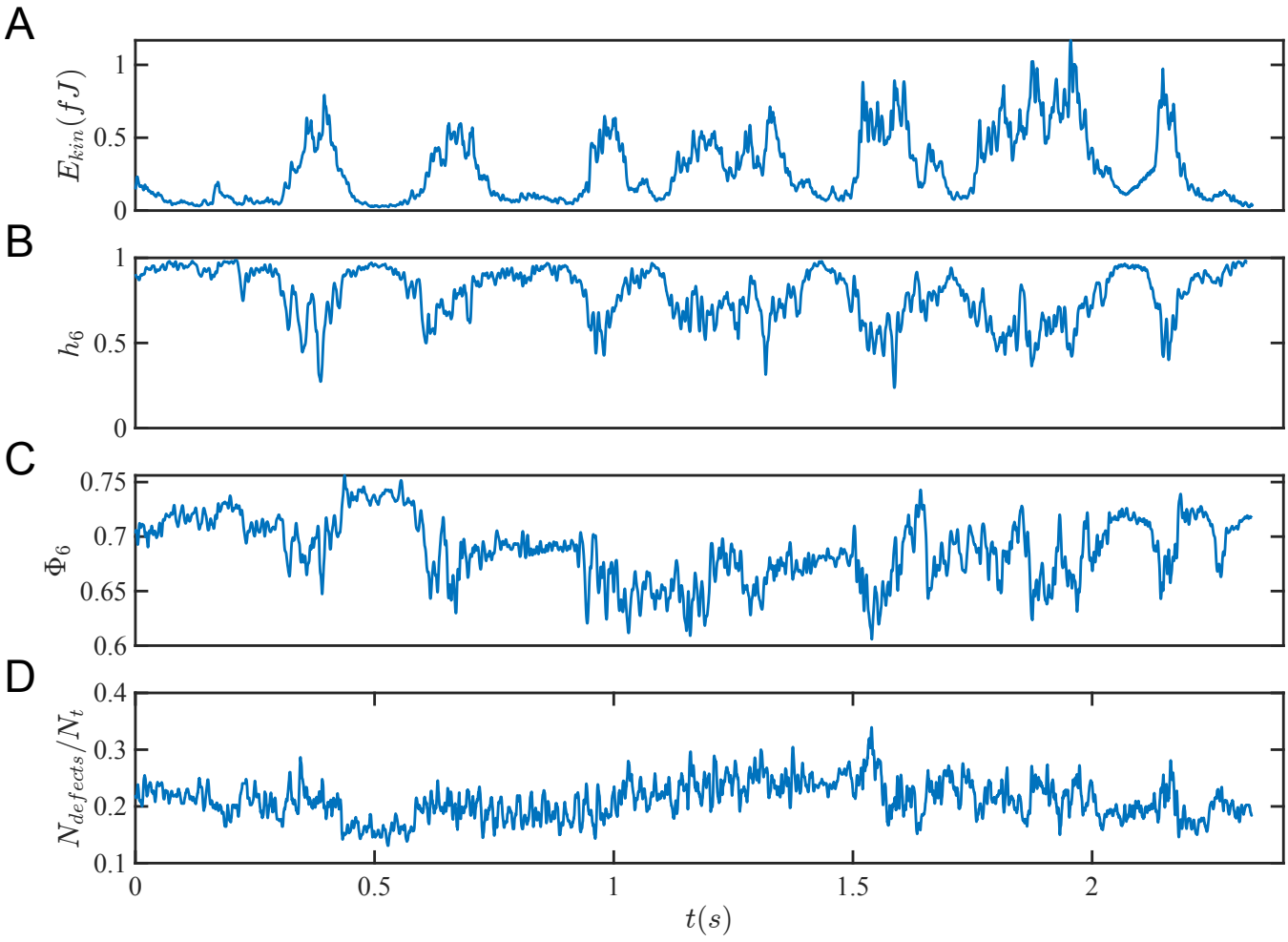

Fig. S12. Intermittent dynamics do not relax disorder in levitated rafts. (*A*) Average kinetic energy per particle as a function of time among intermittent excitation(same as presented in Fig. 5*A* of the main text). (*B*) Structural decorrelation parameter, h_6, as a function of time (same as presented in Fig. 4*D* of the main text). $\Delta t = 10ms$. (*C*) Average local order parameter, Φ_6, as a function of time. (*D*) Percent of defect in the raft, N_{defect}/N_t, as a function of time. N_{defect} and N_t are the number of 5,7 defects and total particle number, respectively.

Langevin perturbations and wait for 2 million simulation time steps dt (1/3 of the total simulation time) before collecting data. Confined by the effectively harmonic potential, the particles form a Wigner crystal at the center of simulation box. The lattice spacing within this crystal is $L = 1.88 = 1.67D$. For all simulation results, distance is normalized with L, energy with $V_B = V_{yukawa}(r = L) = 0.0418$, and time with $t^* = L/ < v >$, where $< v >$ is the average velocity of all particles. We choose the combination of Yukawa repulsion and confining potential so that the structure formed is similar to a raft in the experiment, with an ordered crystal core and a circular boundary. Replacing this combination with Lennard-Jones potential will give us qualitatively the same result, although the defect structure of such a system would not resemble the experimental system.

As shown in Fig. S13*A*, the Wigner crystal has an ordered, defect free triangular lattice for the inner core and a circular boundary; defects mediate between these regions, similar to what we find in the experiment. To quantify the melting behavior of such finite size Wigner crystal, we calculate the mean square displacement (MSD) and bond order correlation parameter for a range of temperatures, shown in Fig. S13*B* and *C*. The MSD traces collapse at the ballistic time scale, but lower k_BT exhibits caging behavior, with a slope smaller than 1 for $t \approx t^*$. For $k_BT/V_B > 0.1$, the cluster is entirely melted and the particles do not experience any caging effects. The experimental liquid MSD (purple dashed line) collapses with the simulation liquid MSD (yellow solid line) for large values of k_BT/V_B. The decay of g_6 is near exponential for $k_BT/V_B > 0.1$, characteristic of a classical 2D liquid. For $k_BT/V_B < 0.04$, g_6 plateaus to a constant value above 0.9, a signature of the crystal state. Between the crystal and liquid, the system does not exhibit a well-defined hexatic (algebratic) decay due to the finite size of the system.

As discussed above, there exists a radial dependence to local order decay in experiments. We now look in simulation at three intermediate temperatures, $k_BT/V_B = 0.05$, 0.08, and 0.1 in more detail to understand the finite size effect in the thermal system. We bin every particle according to its relative radial position within the raft (r/R) as shown in Fig. S13*D-F*. For k_BT=0.05, the inner core of the raft is still a crystal, with little rearrangement, while the edge is in a liquid state (because of weaker confinement). At slightly higher k_BT, the inner core also exhibits substantial decay, although only at a much larger time scale than the outer edge. Eventually, at sufficiently high k_BT, the entire cluster melts and behaves more homogeneously

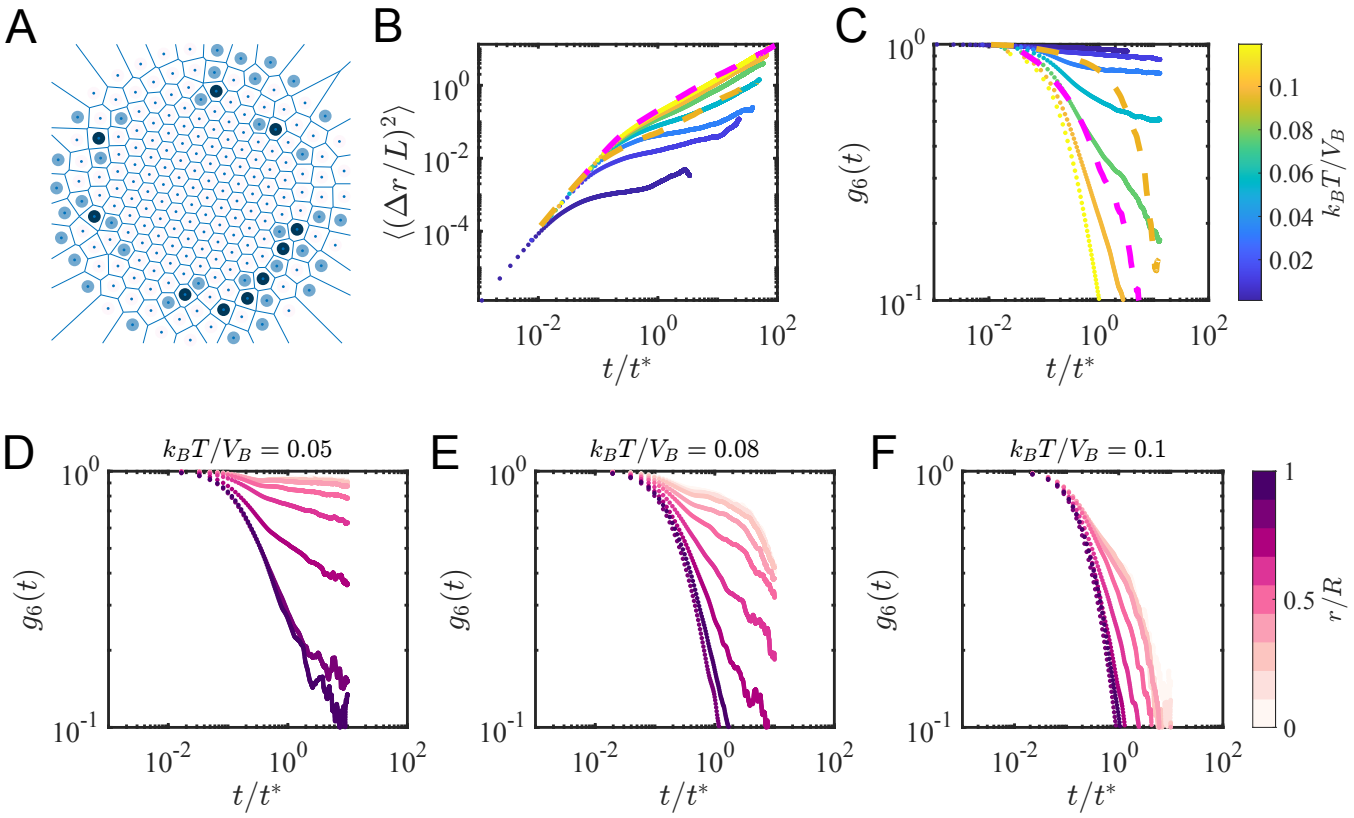

Fig. S13. Properties of a Wigner crystal in thermal bath. (*A*) Low-energy structure of a Wigner crystal at $k_BT/V_B = 0$, shown via a Voronoi construction. 5,7 defects are colored in light and dark blue, respectively. (*B*) Normalized mean square displacement $\langle(\Delta r/L)^2\rangle$ as function of time for different k_BT values. Purple and orange dashed line represent experimental traces for liquid ($p_{ac} = 957Pa$) and intermittent dynamics ($p_{ac} = 848Pa$), respectively. (*C*) Bond order parameter decorrelation as a function of time for different k_BT values. Systems with larger k_BT decay faster. (*D-F*) Bond order parameter decorrelation for different radial positions r/R, at k_BT/V_B=0.05, 0.08, and 0.1, respectively. These systems are in partially melted mixed phase with outer layer more liquid-like and inner layer more solid-like.

(Fig. S13*F*).

Can the experimental system be compared to an equivalent simulated thermal system? To find an appropriate effective temperature for comparison with experiment, we first take k_BT_{eff} as the average in-plane kinetic energy per particle, $\langle E_{kin}\rangle$ and calculate V_B by integrating the radial force obtained from LBM simulation shown in Fig. 2*C* of the main text. The force can be non-dimensionalized with experimental parameters. Using $D = 50\mu m$ and $p_{ac} = 1000Pa$, the bonding energy is found as $V_B = 3 \times 10^{-13}$ J. The k_BT_{eff}/V_B for liquid and intermittent state are respectively 0.01 and 8×10^{-4}, both of which are at least an order of magnitude smaller than the corresponding states for simulations. Thus, we conclude that it is not appropriate to compare the two system with normalized kinetic energy.

Nevertheless, we can instead choose a k_BT/V_B value that gives a similar qualitative structural order decorrelation behavior. To compare with the experimental liquid-like phase, we choose $k_BT/V_B = 0.12$, at which the decay of $g_t(t)$ is exponential, similar to the classical 2D liquid, and the decorrelation time τ/t^* in the bulk is the same as that for the experimental liquid state (purple dashed line, Fig. S13*C*). Although the thermal Wigner crystal does not exhibit any intermittent behavior, we choose $k_BT/V_B = 0.04$ (third lowest k_BT/V_B) for comparison to the experimental intermittent dynamics as the Bond order decorrelation parameters $g_6(t)$ both decay to nearly the same value at $t = t^*$. At this temperature the Wigner crystal is partially melted and in a mixed-phase state between the crystal and liquid. The Bond order correlation parameter $\Phi_6(t-\Delta t)\cdot\Phi_6(t)$ is calculated for every particle in the system with $\Delta t = t^*/3$, similar to the value of Δt used to calculate h_6 for experimental system, as shown in Fig. 4*D* of the main text. By classifying $\Phi_6(t-\Delta t)\cdot\Phi_6(t) > 0.9$ as crystal, $P_{crys} = 0.68$; a similar P_{crys} was found for experimental intermittent dynamics. Although P_{crys} for simulation is calculated spatially, and the experimental value is derived temporally, this particular simulation system is as analogous to the intermittent experimental behavior as possible (yellow dashed line, Fig. S13*C*). Therefore, we choose the system with $k_BT/V_B = 0.04$ to compare with the experimental intermittent dynamics, as shown in Fig. 5*C-E* of the main text.

It is important to note that although the value of k_BT/V_B in the experimental system is orders of magnitude smaller, the particle mobility is comparable to that of the simulation. This is a result of the correlated motion that we have shown in Fig. 5 of the main text. As particles in levitated rafts can uncage easily due to hydrodynamic coupling, little energy is needed for particles to have similar mobility.

14. Removal of Global Translation and Rotation

To remove global translation of the raft from individual particles, we perform the following operations.

$$\vec{r_i^{\,r}}(t) = \vec{r_i^{\,t}}(t) - \langle \vec{r_i^{\,t}}(t) \rangle_N, \quad [2]$$

where $\vec{r_i^{\,t}}(t) = (x_i^{raw}(t), y_i^{raw}(t))$, $x_i^{raw}(t)$ and $y_i^{raw}(t)$ are the xy positions of particle i at time t obtained from particle tracking, $\langle \vec{r_i^{\,t}}(t) \rangle_N$ is the average of $\vec{r_i^{\,t}}(t)$ over all particles N in the system. We perform this operation for all time t before any further operations. This step makes sure that the center of the raft at all time t is centered at the $\vec{r} = (0, 0)$, thereby removing any global translation.

In order to subtract the global rotation of the raft, we aim at finding the angle $\Delta\theta(t)$, which describes the angle of rotation from time $t - \Delta t$ to t, where $\Delta t = 0.33ms$. This can be achieved by minimizing the following cost function $L_t(\Delta\theta)$ with respect to $\Delta\theta$ (10).

$$L_t(\Delta\theta) = \sum_{i=1}^{N} |P_{rot}(\Delta\theta)\vec{r_i^{\,r}}(t) - \vec{r_i^{\,r}}(t - \Delta t)|^2, \quad [3]$$

where $\vec{r_i^{\,r}}(t)$ is the position of particle i at time t after the global translation has been removed, and $P_{rot}(\Delta\theta)$ is the rotation operator defined as

$$P_{rot}(\Delta\theta) = \begin{bmatrix} cos(\Delta\theta) & -sin(\Delta\theta) \\ sin(\Delta\theta) & cos(\Delta\theta) \end{bmatrix}, \quad [4]$$

which takes the position of the particles counterclockwise by an angle $\Delta\theta$. The angle $\Delta\theta(t)$ is calculated for all t. The global rotation can then be subtracted with the following operation

$$\vec{r}_i(t) = \prod_{t'=1}^{t} P_{rot}(\Delta\theta(t'))\vec{r_i^{\,r}}(t). \quad [5]$$

$\vec{r}_i(t)$ is then used for any subsequent analysis.

Movie S1. Bottom view of an acoustically driven cluster. The acoustic pressure is 822 Pa. Playback speed is 1/100 of the real time. The cluster is in the crystal-like state. Scale bar corresponds to $100\mu m$**.**

Movie S2. Bottom view of an acoustically driven cluster. The acoustic pressure is 984 Pa. Playback speed is 1/100 of the real time. The cluster is in the liquid-like state. Scale bar corresponds to $100\mu m$**.**

Movie S3. Side view of an acoustically driven cluster. The acoustic pressure is 984 Pa. Playback speed is 1/100 of the real time. The cluster is in liquid-like state. Scale bar corresponds to $100\mu m$**.**

Movie S4. Bottom view of an acoustically levitated raft exhibiting intermittent dynamics. The acoustic pressure is 845 Pa. Playback speed is 1/10 of the real time. The movie corresponds to 2.7 seconds in real time. Scale bar corresponds to $100\mu m$**.**

Movie S5. Bottom view of an acoustically levitated raft exhibiting intermittent dynamics. The acoustic pressure is 845 Pa. Playback speed is 1/100 of the real time. The movie corresponds to 0.27 seconds in real time. Scale bar corresponds to $100\mu m$**.**

References

1. MX Lim, A Souslov, V Vitelli, HM Jaeger, Cluster formation by acoustic forces and active fluctuations in levitated granular matter. *Nat. Phys.* **15**, 460–464 (2019).
2. J Rudnick, M Barmatz, Oscillational instabilities in single-mode acoustic levitators. *Acoust. Soc. Am. J.* **87**, 81–92 (1990).
3. MA Andrade, FC Buiochi, J Adamowski, Finite element analysis and optimization of a single-axis acoustic levitator. *IEEE Transactions on Ultrason. Ferroelectr. Freq. Control.* **57**, 469–479 (2010).
4. D Fabre, J Jalal, JS Leontini, R Manasseh, Acoustic streaming and the induced forces between two spheres. *J. Fluid Mech.* **810**, 378–391 (2017).
5. F Rouyer, N Menon, Velocity fluctuations in a homogeneous 2d granular gas in steady state. *Phys. Rev. Lett.* **85**, 3676–3679 (2000).
6. K Zahn, G Maret, Dynamic Criteria for Melting in Two Dimensions. *Phys. Rev. Lett.* **85**, 3656–3659 (2000).

7. AL Thorneywork, JL Abbott, DG Aarts, RP Dullens, Two-Dimensional Melting of Colloidal Hard Spheres. *Phys. Rev. Lett.* **118**, 158001 (2017).
8. JS Olafsen, JS Urbach, Two-dimensional melting far from equilibrium in a granular monolayer. *Phys. Rev. Lett.* **95** (2005).
9. JA Anderson, J Glaser, SC Glotzer, Hoomd-blue: A python package for high-performance molecular dynamics and hard particle monte carlo simulations. *Comput. Mater. Sci.* **173**, 109363 (2020).
10. KS Arun, TS Huang, SD Blostein, Least-Squares Fitting of Two 3-D Point Sets. *IEEE Transactions on Pattern Analysis Mach. Intell.* **PAMI-9**, 698–700 (1987).